

# A novel method of micro-tomography geometric angle calibration with random phantom

Haocheng Li<sup>a,b</sup>, Wei Hong<sup>a,\*</sup>, Yu Liu<sup>a</sup> and Xuanqin Mou<sup>a</sup>

<sup>a</sup>*Institute of Image Processing and Pattern Recognition, School of Electronic and Information Engineering, Xi'an Jiaotong University, China*

<sup>b</sup>*Department of Computer Science and Engineering, The Chinese University of Hong Kong, China*

Received 23 July 2016

Revised 16 December 2016

Accepted 22 January 2017

**Abstract.** The objective of this study is to develop and test the feasibility of applying a machine learning method for geometry calibration of angles in micro-tomography systems. Increasing importance of micro-tomography systems are manifested with escalating applications in various scenarios including but not limited to oral and maxillofacial surgery, vascular and intervention radiology, among other specific applications for purposes of diagnosis and treatments planning. There is possibility, however, actual pathology is confused by artifact of tissue structures after volume reconstruction as a result of CT construction errors. A Kernel Ridge Regression algorithm for micro-tomography geometry estimation and its corresponding phantom is developed and tested in this study. Several projection images of a rotating Random Phantom of some steel ball bearings in an unknown geometry with gantry angle information were utilized to calibrate both in-plane and out-plane rotation of the detector. The described method can also be expanded to calibrate other parameters of CT construction effortlessly. Using computer simulation, the study results validated that geometry parameters of micro-tomography system were accurately calibrated.

**Keywords:** Kernel ridge regression, cone beam, computed tomography, geometry calibration

## 1. Introduction

Micro-tomography ( $\mu$ CT) is more portable, flexible [1], inexpensive, quicker and requiring lower radiation dose [2] comparing with CT, which helps numerous applications in image-guided radiation therapy (IGRT) in recent years. Among every picture series of volunteers and patients captured by CT since 1983 [3], it keeps challenging to utilize  $\mu$ CT in IGRT because of the trade-off between image quality, emission dose, and scanning time [4]. The three-dimensional (3D) volume data sets generated by  $\mu$ CT systems are reconstructed from a number of tomographic images projected surrounding the rotating gantry system which locates between X-ray source and scanner [5]. Characterizing geometric relationship parameters of the x-ray source and detector constitutes a geometric calibration for the  $\mu$ CT

---

\*Corresponding author: Wei Hong, Institute of Image Processing and Recognition, School of Electronic and Information Engineering, Xi'an Jiaotong University. No.28, Xianning West Road, Xi'an, Shaanxi 710049, P.R. China. Tel.: +86 29 18092702038; E-mail: weihong@mail.xjtu.edu.cn.

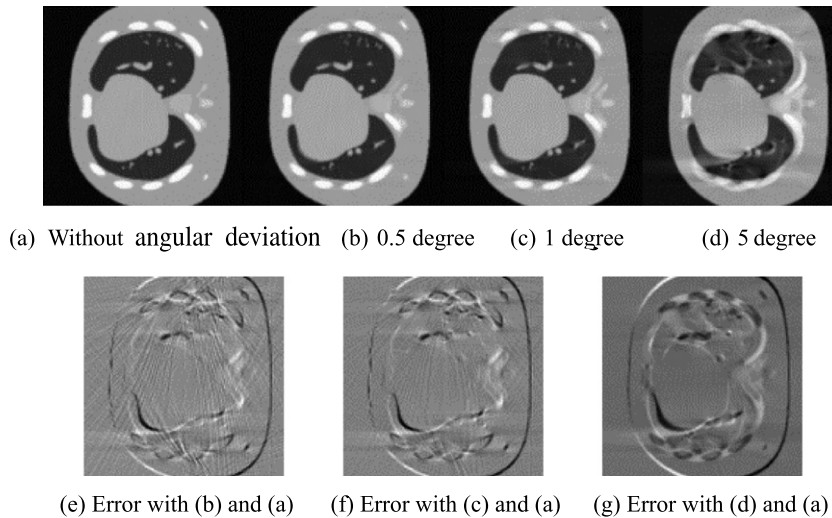


Fig. 1. Reconstruction image and residual error image.

system, and errors in this process give rise to image artefacts such as blur, distortion, and streaks. To have the artifact avoided and to have the volume data sets reassembled accurately, the system geometric parameters are essential but hardly mechanically accessible.

For example, an experiment has been done to better illustrate the artefacts. FDK methods are used in this experiment of cone beam projection. The size of the phantom is  $143 \times 143 \times 143$  while the size of reconstruction slides is  $136 \times 136$ . Both distances from the center of the phantom to the x-ray source and scanner plane are 300. All units are a pixel. The middle of horizontal slides (i.e.  $XoY$ plane) is the least affected by scanner tilt and rotation. Reconstructed images with and without slight tilt and rotation of scanner plane at this slide are used as comparison objects in Fig. 1. If the residual error in the middle slide is not acceptable, error in other slides cannot be less significant. The Fig. 1a is a reconstructed image without tilt or rotation (i.e. control image). Figure 1b, 1c and 1d are reconstructed images with tilt and rotation of 0.5, 1, 5 degrees on all of x, y, z-axes respectively. Figure 1e, 1f and 1g show the residual error between reconstructed image without tilt or rotation and images with 0.5, 1, 5-degree tilt and rotation respectively. Observed from figures, reconstructed images are remarkably different from control image and there are distortions and artefacts. With the increasing of tilt and rotation, distortions and artefacts are more significant. This effect is illustrated in residual images as well. The PSNR between Fig. 1(b) and 1(a) is 110.95. The PSNR between Fig. 1(c) and 1(a) is 105.64. The PSNR between Fig. 1(b) and 1(a) is 94.74.

Actually, even the tilt or rotation is less than 1 degree, there are distortions and artefacts as well which potentially cause a false diagnosis. Therefore, if high precision is required by applications of micro-tomography efforts on eliminating them are necessary. Since obvious tilt or rotation can be detected by mechanical methods, a novel measure of slight tilt and rotation is proposed by this work in order to improve the accuracy of reconstruction and to fetch ideal reconstructed images.

Recently, Brown [6] proposed a polynomial representation instead of a precise analytic expression of both radial and tangential artifact on photographs. Hence this method is somehow speculative dealing with reduction of distortion. Zhang gave an adaptable method to calibrate the intrinsic and extrinsic parameters of cameras easily. However, Zhang deployed the method come up by Brown while dealing with radial distortion [7]. Fitzgibbon presented an efficient method for fitting ellipses to scattered data by normalizing the algebraic distance subject to the constraint  $4ac - b^2 = 1$  [8], which stimulated a series of methods which calibrate the parameters analytically. One of the inspired solutions was provided

by Noo which determined calibration geometry algebraically as it traced two ellipses of spherical objects [9]. Noo's method as well as its other extensions had loss of generality as it assumed that the detector is parallel with the revolution axis of gantry [10]. Making use of a calibration phantom which consisted of a precise positioning of 24 metal ball bearings (BBs) embedded in a cylindrical plastic phantom, Cho developed a more general algebraic algorithm for estimating these geometric parameters [11] but the  $25\mu\text{m}$  machining tolerances of arrangement might be difficult to satisfied. Even an anthropomorphic head phantom with a tungsten wire and lead BB is required by Ouadah [12]. Yang purposed a high-precision calibration method for  $\mu\text{CT}$  system without precise information about the phantom [13]. Rough manual measurement of distance between BBs, however, was still acquired. Lee presented a novel algorithm to calibrate and register a  $\mu\text{CT}$  system with an additional 3D optimal (red green blue depth, RGBD) camera utilizing a calibration phantom which consists of three tubes in different heights, lengths, and orientations [14] while an RGBD camera involved in calibration and not all  $\mu\text{CT}$  system was deployed with an RGBD camera.

In this study, a method for calibrating geometric parameters of  $\mu\text{CT}$  is discussed which requires several projections of a Random Phantom of ball bearings and angle of gantry system. The robustness of this method is guaranteed by computer simulation that no information about the phantom is required to determine the parameters.

## 2. Geography and phantom

### 2.1. Geography

Without loss of generality, we assume that the flat panel detector and the source of X-ray are stable while the gantry system is rotatable. The detector is assumed not to be spatially distorted. It is also convenient to introduce three right-handed dimensional Cartesian coordinate systems named under X-ray source ( $s$ ), virtual scanner ( $v$ ) and real scanner ( $r$ ) as Fig. 2 suggested. Random Phantom which is the designed calibration instrument, purposed patients as well as the rotatable gantry system are valued under X-ray source coordinate system. The  $z$  axis of the X-ray source coordinate system ( $z^s$ ), is parallel with the rotation axis of gantry system. Without loss of generality, point the  $x^s$  axis at the gantry angle of 0 so that  $y^s$  axis is obviously pointing at the gantry angle of 90.

The virtual scanner coordinate system is utilized to model an ideal scanner. Piercing point ( $P_p^s$ ), which is the origin of the virtual scanner coordinate system, is located at the projection point of the center of gantry system. The direction of the  $y^v$  axis is oriented anti-parallel to the  $z^s$  axis of the X-ray source coordinate system while the  $x^v$  axis is perpendicular to the vector from the piercing point to the source point. With the possible tilting ( $\theta$  or  $\phi$ , around the  $x^v$  or  $y^v$  axis) and rotation ( $\eta$ , around the

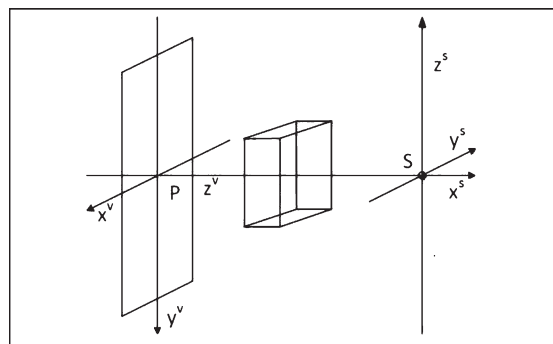


Fig. 2.  $\mu\text{CT}$  System.

$z^v$  axis) from the virtual scanner coordinate system, the real scanner coordinate system is defined. A position vector ( $P^v$ ) in the virtual scanner coordinate system can be easily transformed to one ( $P^r$ ) in the real scanner coordinate system through the beneath formula:

$$\left\{ \begin{array}{l} P^r = R_i^r P^i, \\ R_i^r = \begin{bmatrix} 1 & 0 & 0 \\ 0 & c_z & s_z \\ 0 & -s_z & c_z \end{bmatrix} \begin{bmatrix} c_x & s_x & 0 \\ -s_x & c_x & 0 \\ 0 & 0 & 1 \end{bmatrix} \begin{bmatrix} c_y & 0 & s_y \\ 0 & 1 & 0 \\ s_y & 0 & c_y \end{bmatrix}, \\ c_x = \cos \theta, \\ s_x = \sin \theta, \\ c_y = \cos \phi, \\ s_y = \sin \phi, \\ c_z = \cos \eta, \\ s_z = \sin \eta. \end{array} \right. \quad (1)$$

The X-ray projection on the scanner ( $P_d^s$ ) of an object in the X-ray source coordinate system ( $P^s$ ) can be expressed by the following equation:

$$P_d^s = \frac{R_z \cdot (P_p^s - P_s^s)}{R_z \cdot (P^s - P_s^s)} \cdot P^s + P_s^s \quad (2)$$

where  $P_s^s$  is the position vector of the X-ray source. Five characters are used to describe the  $\mu$ CT system geometry in this paper: gantry position  $P_g^s = [X_g^s, 0, 0]^T$ , piercing point  $P_p^s = [X_p^s, 0, 0]^T$ , tilting  $\theta$ ,  $\phi$  and rotation  $\eta$  while other parameters which are assumed as 0 can also be covered after the expand of this study.

## 2.2. Random phantom

The phantom for calibration comprises a random arrangement of several metal BBs embedded in a cubic plastic model whose length of each side is 100 mm. The size of cube and number of BBs can be altered within the compatibility of the algorithm. More BBs, however, may cause problems of performance during calibration. Another trade-off which should be considered is between phantom size and geometric precision and accuracy. In order to maximize robustness of calibration, the diameter of each BB should be large enough to include a large number of pixels and to exhibit high contrast yet small enough to avoid overlapping with neighboring BBs when projected [11]. Finally, to make sure that each BB is visible in every photograph of scanner, the calibration phantom is supposed to be placed at the approximate center of the gantry system.

## 3. Theory

### 3.1. Kernel ridge regression

The Support Vector (SV) method is a universal tool for solving not only linear but also nonlinear multidimensional function estimation problems. To begin with, it was designed for solving problems of pattern recognition where one selects some subset of training data called the SVs to find a set of classification rules with strong generalization ability. This leads to a representation of decision trees which are a linear expansion on a basis whose elements are nonlinear functions characterized

by the SVs [15]. We apply SV method handle the problem of calibration. In this case of regression, maintaining all the main features to generate a non-linear function by a linear learning machine in a kernel-induced feature space while the capacity of the system is controlled by a parameter that does not depend on the dimensionality of the space [16]. We consider the following perfect-information protocol of on-line regression:

---

**Protocol 1.** Online Regression Protocol

---

**for**  $t := 1, 2, \dots$  **do**  
 Reality announces  $x_t \in X$   
 Learner predicts  $\hat{y}_t \in \mathbb{R}$   
 Reality announces  $y_t \in \mathbb{R}$   
**end for**

---

We consider  $F$  is a linear set of functions  $f(x)$  defined in set  $X$ .  $F$  is supposed to be either a *real* or *complex* class, in hence it accepts multiplication of complex constants. The norm for  $f \in F$  is defined following:

**Definition 1.** The norm for  $f \in F$  is given by a quadratic form,

$$\|f^2\| = Q(f), \tag{3}$$

where for any constants  $\xi_1, \xi_2 \in \mathbb{C}$  and any function,  $f_1, f_2 \in F$ ,

$$Q(\xi_1 f_1 + \xi_2 f_2) = |\xi_1|^2 Q(f_1) + \xi_1 \xi_2 (Q(f_1, f_2) + Q(f_2, f_1)) + |\xi_2|^2 Q(f_2), \tag{4}$$

$Q(f_1, f_2) = \overline{Q(f_2, f_1)}$  is the uniquely determined bilinear hermitian form corresponding to the quadratic form  $Q(f)$  [17].

This bilinear form will be denoted by

$$\langle f_1, f_2 \rangle \equiv Q(f_1, f_2) \tag{5}$$

and called the scalar product corresponding to the quadratic metric  $\|f\|^2$ :

$$\|f\|^2 = \langle f, f \rangle. \tag{6}$$

The complete class of  $F$  with the norm,  $\| \cdot \|$ , forms a Hilbert space of  $X$ .

**Definition 2.** A function  $K(x_1, x_2)$  of  $x_1, x_2 \in X$  is called a *reproducing kernel (RK)* of  $F$  if

$$\forall x_2 \in X, K(x_1, x_2) \in F \tag{7}$$

$$\forall x_2 \in X, \forall f \in F, f(x_2) = \langle f(x_1), K(x_1, x_2) \rangle_F \tag{8}$$

the subscript  $H$  by the scalar product indicates that the scalar product applies to RKHS of  $F$  [18].

We shall suppose the case where the space  $X$  from which the input vector  $x_t$  are drawn is an arbitrary set of inputs. Let  $F$  be a reproducing kernel Hilbert space (RKHS) of functions  $X \rightarrow \mathbb{R}$  as a functional Hilbert space with continuous evaluation functional  $f \in F, \forall x \in X$ . According to the Riesz-Fischer theorem:

$$\forall x \in X, \forall f \in F, \exists k_x \in F \langle k_x, f \rangle_F = f(x) \tag{9}$$

Define the kernel  $K : X^2 \rightarrow \mathbb{R}$  of the RKHS  $F$  as  $K(x_1, x_2) = \langle k_{x_1}, k_{x_2} \rangle$  [19]. The optimization problem becomes:

$$\begin{cases} \text{minimize} & a \|f\|_F^2 + \sum_{t=1}^T \xi_t^2 \\ \text{subject} & \xi_t = y_t - f(x_t), t = 1, 2, \dots, T \end{cases} \quad (10)$$

Let  $L_t$  be an  $(n \times n)$  Gram matrix at step  $t$  and  $Y_t$  be the column vector of labels  $y_i$  for  $i = 1, 2, 3, \dots, t$ . we can express the final Kernel Ridge Regression prediction at each step  $T$  in the scalar product mode form [20]:

$$\gamma^T = Y_{T-1}'(aI + L_{T-1})^{-1}k_T \quad (11)$$

where  $k_t$  is the column vector  $K(x_i, x_t)$  for  $i = 1, 2, 3, \dots, t - 1$ .

The following theoretical guarantee of the Kernel Ridge Regression learner is proved [21]:

**Theorem 1.** *The Kernel Ridge Regression algorithm for the learner with  $a > 0$  satisfies, at any step  $T$ ,*

$$\sum_{t=1}^T \frac{(y_t - \gamma_t)^2}{1 + \frac{K(x_t, x_t) - k_t'(aI + L_{t-1})^{-1}k_t}{a}} = \min \left( \sum_{t=1}^T (y_t - f(x_t))^2 + a \|f\|^2 \right), f \in F. \quad (12)$$

### 3.2. Procedure

For the calibration of a  $\mu$ CT system, the rotation of detected object and stationarity of X-ray source and scanner are assumed. Place a random phantom with  $N$  metal BBs nearly at the center of gantry system. Since not all viewing angles of the object are available in practice, divide the flat angle into  $M$  equal part and choice about the center of each part as one of the gantry angle.

After projection, an array of  $M$  digitalized images is exported from the scanner and shadows of each BB can be identified from every radiographic image. Projection positions of BBs are described by the real scanner coordinate system. Due to the stability of 0 value on  $z'$  axis, only two parameters of the positions are counted in the data structure. In conclusion, the data structure is constructed by the Protocol 2.

---

#### Protocol 2. Projection Protocol

---

Initiate  $LLV$  as a list of lists to represent all data

**For**  $m := 1, 2, \dots, M$  **do**

Initiate  $LV$  as a list of vectors to represent data of an image

**For**  $n := 1, 2, \dots, N$  **do**

Initiate  $V$  as a vector of 2 dimensions

Assign the position of shadow to  $V$

Push  $V$  in  $LV$

**end for**

Push  $LV$  in  $LLV$

**end for**

---

Serialize  $LLV$  as a vector of  $x$  features which has  $M \times N \times 2$  dimensions. For each specific  $x$ , the Kernel Ridge Regression learner can get an exact  $y$  with 3 dimensions which can be described as  $[\theta, \phi, \eta]$ . The learner is trained by computer simulation. Due to the lack of computation resource, we

generate only data of 21000 inputs and outputs. Supposed outputs are generated under the following normal distribution:

$$\begin{cases} R_I \sim N(200, 1), \\ R_D \sim N(400, 1), \\ \theta \sim N(0, 1), \\ \phi \sim N(0, 1), \\ \eta \sim N(0, 1), \end{cases} \quad (13)$$

where  $R_I$  is the distance of gantry center from X-ray source and  $R_D$  is the distance of pierce point from X-ray source. The learner fetches 20000 cases randomly for training and uses the rest for testing.

## 4. Simulation

### 4.1. Method

As mentioned above, the BBs in random phantom are supposed to locate far enough with each other to prevent their shadows on scanner from overlapping together. To generate an ideal phantom, we use nearest-neighbor graph (NNG) to validate BBs from a dependently and uniformly chosen set.

Let  $V = \{v_1, v_2, \dots, v_n\}$  be a set of points in  $\mathbb{R}^t$ .

**Definition 3.** The *nearest neighbor* of  $v_i$  is a point  $v_j, j \neq i$ , with minimum Euclidean distance from  $v_i$ . For the uniqueness of the nearest neighbor, the point  $v_j$  is chosen with the maximum index in case of ties and denoted as  $nn(v_i)$ .

**Definition 4.** The *shortest edge* of  $v$  is the directed edge  $e(v) = \langle v, nn(v) \rangle$ .

**Definition 5.** The *nearest-neighbor graph (NNG)*  $NNG(V)$  of a point set  $V$  is the directed graph  $\langle V, E \rangle$  where  $E = \{e(v)|v \in V\}$  [22].

We simply use the distance of shortest edge in NNG to evaluate the priority of a phantom. In this study, we generate 1000 phantoms with independent and uniform BBs and choose the one with the longest distance of shortest edge in NNG as the calibration phantom. During simulation, we choose  $M \in \{3, 4, 5, 6, 7, 8\}$  and  $N \in \{8, 10, 12, 14, 16, 18\}$  to discover the trend of correctness. In order to simulate the practical situation of noise, for each feature in the input array with the unit of millimeter, a  $N(0, 0.01)$  Gaussian noise is added. After that, features are digitalized to precision of 0.1 mm.

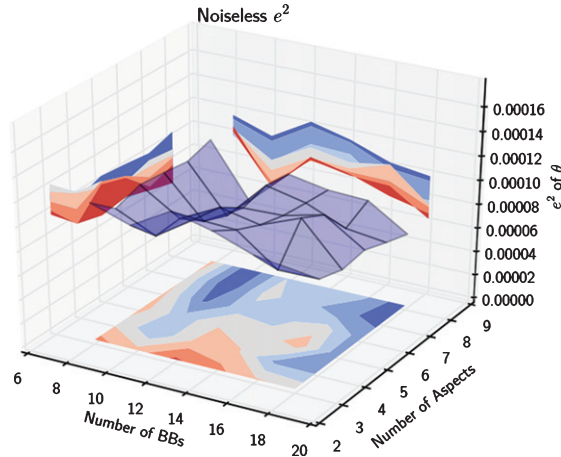
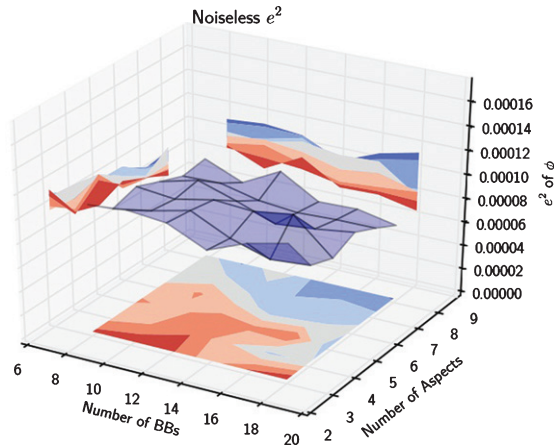
### 4.2. Result

We utilize fraction of variance unexplained to evaluate the accuracy of fitted model.

**Definition 6.** The *fraction of variance unexplained (FVU)*  $e^2$  is defined as:

$$\begin{cases} e^2 = \frac{f}{g} \\ f = E [t_i - p_i]^2 \\ g = E [t_i - \bar{t}]^2 \\ \bar{t} = E [t_i] \end{cases} \quad (14)$$

where  $t_i$  is the true label of each case and  $p_i$  is the predicted label for each case [23].

Fig. 3. Coefficient of Determination of  $\theta$  without Noise.Fig. 4. Coefficient of Determination of  $\phi$  without noise.

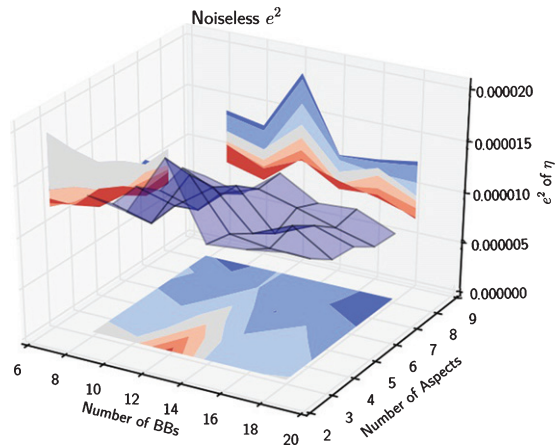
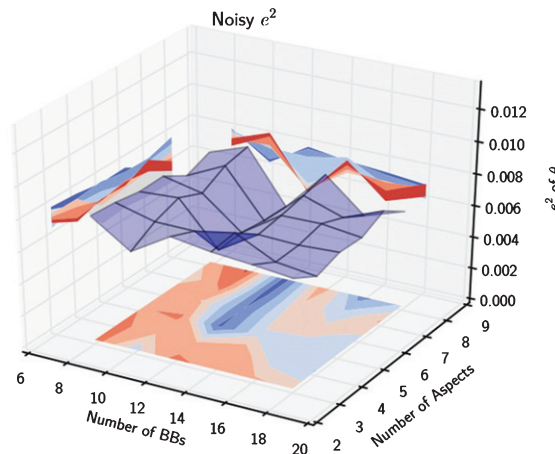
The score can be no negative and can be higher than 1.0. A constant model that always predicted the same label regardless of the input features would get a 1.0 score. FVU of all 3 parameters without condition of noise and digitalization are show in the 3 contour patterns demonstrated in Figs. 3 to 5, respectively.

Generally, it is manifest from the contour figures that with the increment of either number of BBs or number of aspects, FVU between true labels and predicted labels is descending. However, the number of BBs, by contrast, acts with some uncertainty which presents anomalous phenomena. The points of extremal abnormality appear at the same position in fields of different parameters which is  $N \in \{12, 16\}$ .

More specifically comparing between different parameters, use

$$\begin{cases} M = 8, \\ N = 18, \end{cases} \quad (15)$$

as an example, the most precise prediction among the 3 parameters is given by  $\eta$  with less than  $7 \times 10^{-6}$  uncertainty whereas  $\theta$  and  $\phi$  present about  $6 \times 10^{-5}$  uncertainty.

Fig. 5. Coefficient of Determination of  $\eta$  without noise.Fig. 6. Coefficient of Determination of  $\theta$  with Noise.

FVU of all 3 parameters within condition of noise and digitalization are show in the 3 contour figures below: Figs. 6, 7, 8.

Use the same case in Equation 15 as an example, the most precise prediction among the 3 parameters is given by  $\eta$  as well with about  $1 \times 10^{-3}$  uncertainty where as  $\theta$  and  $\phi$  present about  $6 \times 10^{-3}$  uncertainty. Comparing with noiseless cases, uncertainty increases for about 2 orders of magnitude. Furthermore, there are still anomalous phenomena but the points of extremal abnormality may alter from noiseless cases.

#### 4.3. Reconstruction

The result of reconstruction is shown in Fig. 9. The images are reconstructed by Feldkamp-type(FDK) algorithm which projections have been rectified by  $\theta, \phi, \eta$ . Figure 9(a) shows the reconstruction of quite image with rectification. The PSNR between Fig. 9(a) and 1(a) is 224.78. Figure 9(b) shows the reconstruction of noisy image with rectification. The PSNR between Fig. 9(b) and 1(a) is 143.17. Hence, compared with Fig. 1(b), the quality of reconstruction is improved by rectification significantly: quality of quiet image gets an improvement of more than 100 dB while even quality of noisy image gets an improvement of more than 30 dB.

## 5. Discussions and conclusions

Geometry calibration is important to produce high quality medical images in disease detection and diagnosis [24, 25]. For example, Chen et al. reported an iterative locally linear embedding (LLE) based calibration approach to address this challenge under a rigid 2D object assumption [26]. However even if iterative LLE was able to converge, it was not guaranteed that the limitation was the optimized parameters. Comparing with classical methods [10, 11, 13] and recent ones [12, 26], a new machine learning method proposed and tested in this study for  $\mu$ CT geometry calibration is more general and convenient since no information of phantom is required. It is clearly seen from simulation that this study provides a machine learning method that have the ability to present more accurate prediction by acquiring more projection of various aspects.

However, there are still some items which can be improved in further research. First, in current simulation, we use an Intel® Core™ i7-3517U processor with 8GB RAM. The fitting process occupies at last 6GB RAM while handling 20000 cases of data and more RAM is required for more cases or the operating system will not response. Since precision can be ameliorated by additional features and

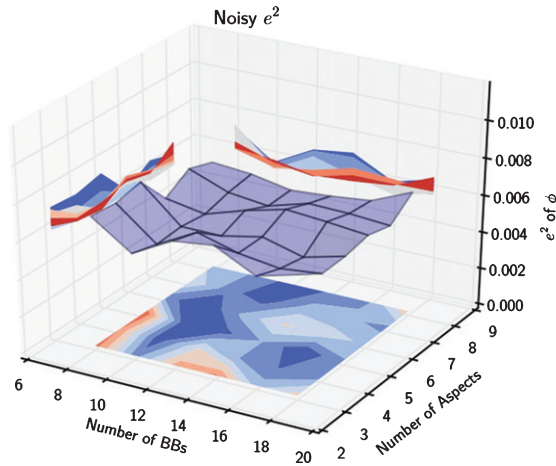


Fig. 7. Coefficient of Determination of  $\phi$  with noise.

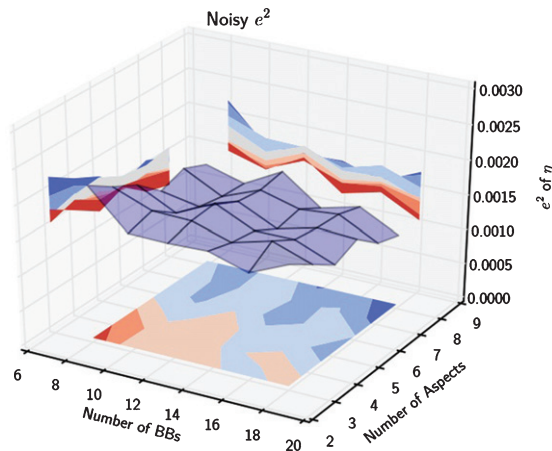


Fig. 8. Coefficient of Determination of  $\eta$  with noise.

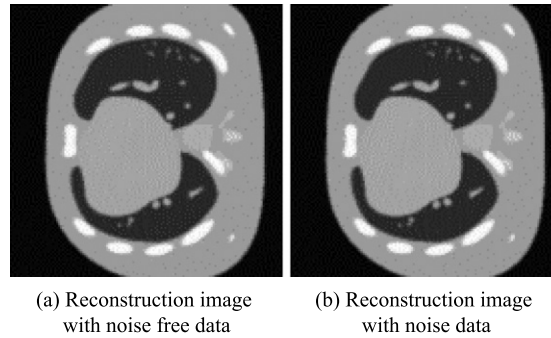


Fig. 9. Reconstruction image which projections have been rectified by  $\theta$ ,  $\phi$ ,  $\eta$ .

extra cases, with more powerful computing machine, more features and cases can be fed to the learning machine and more precise predictions can be expected. Second, supplementary parameters of  $\mu$ CT system can be introduced into this calibration method easily because the learning machine does not rely on any parameter. Third, the correlation is not transparent between  $FVU$  and number of BBs. Simulations of  $N \in \{9, 11, 13, 15, 17, 19\}$  may help solving this problem.

One of the reasons which may cause the greater uncertainty in noisy cases is that the noise and digitalization are at rough estimate. The current estimation is more influential than common situations. In order to solve the problem of misrepresentation of tissue structures caused by errors in  $\mu$ CT construction, a machine learning method is chosen to calibrate  $\mu$ CT system. Kernel Ridge Regression is applied in the calibration and  $FVU$  for  $[\theta, \phi, \eta]^T$  is simulated as  $[6.1 \times 10^{-5}, 6.3 \times 10^{-5}, 6.6 \times 10^{-6}]^T$  and  $[6.1 \times 10^{-3}, 6.6 \times 10^{-3}, 1.0 \times 10^{-3}]^T$  in the noiseless and noisy situation, respectively.

## Acknowledgments

We would like to thank Xuelu Chen for helpful discussion on Hilbert space.

## References

- [1] U. Linsenmaier et al., Three-dimensional CT with a modified C-arm image intensifier: Feasibility, *Radiology* **224**(1) (2002), 286–92.
- [2] G. Omar, Z. Abdelsalam and W. Hamed, Quantitative analysis of metallic artifacts caused by dental metallic restorations: Comparison between four CBCT scanners, *Future Dental Journal* **2**(1) (2016), 15–21.
- [3] W. Swindell et al., Computed tomography with a linear accelerator with radiotherapy applications, *Medical Physics* **10**(4) (1983), 416–420.
- [4] P. Jin et al., 4D cone-beam CT imaging for guidance in radiation therapy: Setup verification by use of implanted fiducial markers, *SPIE Medical Imaging, International Society for Optics and Photonics* 2016, 97862N–97862N.
- [5] X. Zou and Z. Li, Optimization Reconstruction of Spiral Cone-beam CT with Displaced Detector and Increased Pitch, *International Conference on Medicine & Biopharmaceutical* (2016), 427–435.
- [6] D.C. Brown, An advanced reduction and calibration for photogrammetric cameras, *An Advanced Reduction & Calibration for Photogrammetric Cameras* 1964. Air Force Cambridge Research Laboratories, Report No. 64-40.
- [7] Z. Zhang, Flexible camera calibration by viewing a plane from unknown orientations, *Seventh IEEE International Conference on Computer Vision* **1** (1999), 666–673.
- [8] A. Fitzgibbon, M. Pilu and R.B. Fisher, Direct least square fitting of ellipses, *IEEE Transactions on Pattern Analysis & Machine Intelligence* **21**(5) (2000), 476–480.
- [9] F. Noo et al., Analytic method based on identification of ellipse parameters for scanner calibration in cone-beam tomography, *Physics in Medicine and Biology* **45**(11) (2000), 3489–3508.

- [10] F. Zhang et al., Practical geometric calibration for helical cone-beam industrial computed tomography, *Journal of X-ray Science and Technology* **22**(1) (2014), 19–35.
- [11] Y. Cho et al., Accurate technique for complete geometric calibration of cone-beam computed tomography systems, *Medical Physics* **32**(4) (2005), 968–983.
- [12] S. Ouadah et al., Self-calibration of cone-beam CT geometry using 3D–2D image registration, *Physics in Medicine and Biology* **61**(7) (2016), 2613–2632.
- [13] K. Yang et al., A geometric calibration method for cone beam CT systems, *Medical Physics* **33**(6) (2006), 1695–1706.
- [14] S. Lee et al., Calibration of RGBD camera and cone-beam CT for 3D intra-operative mixed reality visualization, *International Journal of Computer Assisted Radiology and Surgery* **11**(6) (2016), 1–9.
- [15] V. Vapnik, S.E. Golowich and A. Smola, Support vector method for function approximation, regression estimation, and signal processing, *Advances in Neural Information Processing Systems* (1996), 281–287.
- [16] N. Cristianini and J. Shawe-Taylor, An introduction to support vector machines and other kernel-based learning methods, *Cambridge University Press*, 2000.
- [17] N. Aronszajn, Theory of reproducing kernels, *Transactions of the American Mathematical Society* **68** (1950), 337–404.
- [18] F. Girosi, An equivalence between sparse approximation and support vector machines, *Neural Computation* **10**(6) (1998), 1455–1480.
- [19] B. Schölkopf and A.J. Smola, Learning with kernels: Support vector machines, regularization, optimization, and beyond, *MIT Press* **16**(3) (2003), 781–781.
- [20] R. Rosipal and L.J. Trejo, Kernel partial least squares regression in reproducing kernel hilbert space, *Journal of Machine Learning Research* **2**(2) (2002), 97–123.
- [21] F. Zhdanov and V. Vovk, Competing with Gaussian linear experts, *Computer Science* 2010.
- [22] D. Eppstein, M.S. Paterson and F. Yao, On nearest-neighbor graphs, *Discrete & Computational Geometry* **17**(3) (1997), 263–282.
- [23] J.H. Friedman, Classification and multiple regression through projection pursuit, *Stanford University*, 1984.
- [24] N.H. Lu, T.B. Chen, K.Y. Liu, et al., Investigated geometrical characteristics and image density of left ventricle of multi-detector computed tomography in early coronary artery disease patients, *Journal of X-ray Science and Technology* **24**(3) (2016), 353–359.
- [25] S. Song, J. Yang, J. Fan, et al., Geometrical force constraint method for vessel and x-ray angiogram simulation, *Journal of X-ray Science and Technology* **24**(1) (2016), 87–106.
- [26] M. Chen, Xi Yan, W. Cong, et al., X-ray CT geometrical calibration via locally linear embedding. *Journal of X-ray Science and Technology* **24**(2) (2016), 241–256.